ELSEVIER

Contents lists available at ScienceDirect

Acta Materialia

journal homepage: www.elsevier.com/locate/actamat



Full length article

Simultaneous high strength and mechanical stability of bcc Nb/Mg nanolaminates



Manish Jain^{a,b}, Krishna Yaddanapudi^c, Anugraha Thyagatur Kidigannappa^b, Kevin Baldwin^d, Marko Knezevic^e, Nathan A. Mara^f, Irene J. Beyerlein^g, Siddhartha Pathak^{h,*}

- ^a Laboratory for Mechanics of Materials and Nanostructures, Empa, Swiss Federal Laboratories for Materials Science and Technology, Feuerwerkerstrasse 39, CH-3602 Thun. Switzerland
- ^b Chemical and Materials Engineering, University of Nevada, Reno, NV 89557, USA
- ^c Department of Materials Science and Engineering, University of California, Davis, CA 95616, USA
- ^d Center for Integrated Nanotechnologies, Los Alamos National Laboratory, Los Alamos, NM 87545, USA
- ^e Department of Mechanical Engineering, University of New Hampshire, Durham, NH 03824, USA
- Department of Chemical Engineering and Materials Science, University of Minnesota, Minneapolis, MN 55455, USA
- g Department of Mechanical Engineering, Materials Department, University of California at Santa Barbara, Santa Barbara, CA 93106, USA
- ^h Department of Materials Science and Engineering, Iowa State University, Ames, IA 50011, USA

ARTICLE INFO

Article history: Received 14 July 2022 Revised 24 October 2022 Accepted 25 October 2022 Available online 30 October 2022

Keywords:
Metal-metal composites
Physical vapor deposition
Interface engineering
Lightweight
Phase transformations
Transmission electron microscopy

ABSTRACT

While bimetallic nanocomposites have demonstrated extraordinary - three to even ten-fold - gains in strength with decreasing layer thickness, their strengths tend to plateau beyond a critical layer thickness. More disappointingly, such increases in strength are almost always accompanied by a decrease in their strains to failure (ductility). In this work we report simultaneous improvements in both strength and mechanical stability of Nb/Mg nanolaminates with decreasing layer thicknesses, a trend seldom reported in nanolaminates consisting of pure metals. Using micro-pillar compression and nanoindentation experiments we show that physical vapor deposited (PVD) Nb/Mg nanolaminates that contain a body center cubic (bcc) Mg pseudomorphic phase demonstrate a >60% increase in strength and a >80% increase in strain to failure over those containing the hexagonal close packed (hcp) Mg phase. Instead of a strength plateau, the hcp-to-bcc phase transition in Mg results in a renewed strengthening regime in the nanolaminate caused by the change to a coherent interface from an incoherent one, along with a concurrent increase in strain-to-failure due to the introduction of a more plastically isotropic bcc material from an anisotropic hcp structure. Using high resolution transmission electron microscopy (HR-TEM) we also demonstrate the presence of a thin layer of bcc Mg at the Nb/Mg interface at larger layer thicknesses when Mg is predominantly hcp. Our results suggest that the increases in strain to failure in the Nb/Mg nanolaminates with decreasing layer thicknesses can be corelated to the approximate volume fraction of the pseudomorphic bcc Mg present in the layers.

© 2022 Acta Materialia Inc. Published by Elsevier Ltd. All rights reserved.

1. Introduction

Metal-metal nanoscale multilayered composites have shown extraordinary improvements in strength when their individual layer thicknesses are reduced to 1–2 nm [1,2]. However, along with the 'smaller is stronger' effect, most multilayered systems also show a corresponding reduction in the instability strain (also called the strain to failure) with decreasing layer thicknesses, crystal di-

ameter, or grain size [3,4], making the composite less formable. These very finely nanolayered materials usually fail due to the formation of a localized shear band [5,6] or exhibit a greater tendency for strain localization [7–10]. Multiple approaches have been attempted in the literature to simultaneously improve both the strength and ductility of layered nanocomposites. A majority of these efforts have typically utilized constituent phases that possess significant differences in elastic modulus, strength, and ductility, such as metal-ceramic nanolaminates that show improved strength and ductility relative to their non-layered counterparts [11–15], and other functionally graded composite systems that demonstrate non-conventional deformation mechanisms [16,17].

^{*} Corresponding author at: 2220BP Hoover Hall, 528 Bissell Rd, Department of Materials Science and Engineering, Iowa State University, Ames, IA 50011, USA. E-mail address: pathak@iastate.edu (S. Pathak).

In recent work we have employed a different, more radical approach to overcoming this problem, which utilizes pseudomorphic phase transformation [18,19] in a multilayered nanocomposite. We explored the synthesis of a nanolaminate consisting of magnesium (Mg) and a second metal niobium (Nb), with the final goal of enhancing both the strength and ductility of the composite [20]. The constituent Mg phase is plastically anisotropic and not ductile due to its inherent hexagonal closed pack (hcp) structure. However, by encouraging a pseudomorphic phase transformation of Mg within the Mg/Nb multilayers, the hcp structure of Mg was transformed to a less anisotropic and more ductile body center cubic (bcc) structure at ambient pressures [21–23]. The result is a low energy, coherent bcc Nb/Mg interface. The critical layer thickness for stabilizing the pseudomorphic bcc Mg phase (above which the metal reverts back to its traditional hcp structure under ambient conditions) was found to be around 7-8 nm from experimental observations [24]. This value is somewhat larger than the critical layer thickness of 4.2 nm for Mg predicted using an analytical model with density functional theory (DFT) information [23], or 5 nm from direct thermodynamic calculations [25]. Initial micro-pillar compression and indentation experiments have shown that the Nb/Mg nanolaminates with lower layer thicknesses (~5 nm, where Mg is bcc) was 50% stronger and twice as ductile than that of the hcp Mg nanolaminate with larger layer thicknesses (\sim 50 nm) [20]. Much of the strengthening can be attributed to the confinement on dislocation motion imposed by the reduced layer thickness. A recent modeling study has suggested that the pseudomorphic bcc Mg phase additionally contributes to nanolaminate strength by increasing the slip strengths of the (111) dislocations compared to the relatively soft basal slip in the hcp Mg, even though the coherent bcc Nb/Mg interfaces pose less resistance to dislocation motion than the incoherent bcc Nb/hcp Mg interface [26]. More remarkably, the nanolaminates with the meta-stable pseudomorphic bcc Mg phase were also shown to be highly stable under extremes of temperature [20] and applied stresses of up to 60 GPa in a diamond anvil cell [24]. It suggests that bcc Mg is a highly attractive pseudomorphic phase from a structural viewpoint and may operate by similar deformation mechanisms as traditional bcc metals and may be just as ductile and formable. This is an exciting concept, particularly for pure Mg, which is an intrinsically lightweight material but disappointingly anisotropic and brittle at room temperature due to its hcp structure and profuse twinning. Compared to conventional ways that are typically utilized to stabilize bcc Mg, such as high pressures (50 ± 6 GPa) [27,28], or alloying [29–31], our multilayered design approach is the only technique that enables pure Mg to exist in the pseudomorphic bcc phase at ambient pressures and temperatures [20,21].

The initial experiments described above were conducted on primarily two distinct Nb/Mg layer thicknesses, 5 vs. 50 nm, and it is difficult to decouple the effects of changing layer thickness, crystal structure, and interface structure (coherent bcc/bcc vs. semi-coherent hcp/bcc) from this limited sample size. In this work, we investigate an expanded range of Nb/Mg nanolaminates with five different (average) individual layer thicknesses - 1.7 nm (Nb)/1.9 nm (Mg), 5.5 nm (Nb)/5.5 nm (Mg), 8.4 nm (Nb)/7.6 nm (Mg), 14.1 nm (Nb)/18.9 nm (Mg) and 76.6 nm (Nb)/62.6 nm (Mg), see Table 1. These layer thicknesses were specifically chosen so that the simultaneous effects of layer thickness, crystal structure and interface type could be compared separately. Consequently, the Mg phase in the two smaller multilayer thicknesses is in its pseudomorphic bcc structure (1.7 nm (Nb)/1.9 nm (Mg), and 5.5 nm (Nb)/5.5 nm (Mg)), whereas Mg in the two larger thicknesses is in its traditional hcp structure (14.1 nm (Nb)/18.9 nm (Mg) and 76.6 nm (Nb)/62.6 nm (Mg)). Intriguingly, at the intermediate multilayer thickness, the Mg phase comprises a mix of hcp Mg and bcc Mg phases (8.4 nm (Nb)/7.6 nm (Mg)). The mechanical properties of the multilayers were investigated using indentation and micro-pillar compression experiments. These findings were correlated with the structure information obtained using high resolution transmission electron microscopy (HR-TEM) techniques to determine the exact layer thicknesses and crystal structures of the deposited Mg and Nb layers. We show that under physical vapor deposition (PVD) conditions, the pseudomorphic transformation in Mg is not abrupt. Rather, the transformed pseudomorphic bcc Mg phase initiates from the Nb/Mg interface and extends a finite distance into the original hcp phase. Thus, even at larger layer thicknesses (when Mg is predominantly hcp), there exists a thin layer of bcc Mg at the Nb/Mg interface. Our analysis suggests that the increases in strain to failure - and hence the increased ductility with decreasing layer thicknesses - in the Nb/Mg nanolaminates can be correlated to the approximate volume fraction of the pseudomorphic bcc Mg present in the layers.

2. Experimental methods

Nb and Mg multilayered nanocomposites with five different average layer thicknesses – Nb/Mg 1.7 nm/1.9 nm, 5.5 nm/5.5 nm, 8.4 nm/7.6 nm, 14.1 nm/18.9 nm and 76.6 nm/62.6 nm – were deposited using DC magnetron sputtering with 2.67×10^{-6} Pa base pressure, 0.4 Pa process pressure, and 300 W of power on a 50.8 mm target in a sputtering-evaporation PVD chamber (AJA International Inc., Scituate, Massachusetts). During deposition, the difference between the plasma potential and the floating potential is estimated to be around \sim 14 V based on the values reported in literature [32] for the Ar gas plasma used for deposition.

Table 1 summarizes the average±standard deviation of the measured layer thicknesses. Nb was the first layer to be deposited, while Mg the last deposited layer in the multilayered nanocomposites. The deposition rates were 0.22 nm/sec for Nb and 0.83 nm/sec for Mg. The total film thickness for all multilayers was approximately 5 μm, except for the Nb/Mg 1.7 nm/1.9 nm layer thickness for which the total film thickness was around 1.6 µm. Films were deposited on Si substrates with deposition parameters chosen to minimize residual stresses. The substrate was not heated or biased during the deposition. However, even at room temperature deposition, substrate temperature is estimated to be in the range of \sim 100–130 °C due to plasma heating conditions [33,34]. Among the various substrate materials considered (single crystal substrates of MgO, sapphire, and Si, each with different crystal orientations) the Si substrates were found to have the lowest (compressive) residual stresses of around 150-200 MPa. The final layer thicknesses and the structural orientations of these as-deposited Nb/Mg films were examined by IEOL IEM 2100F-AC scanning/transmission electron microscope (STEM/TEM) operating at 200 keV. The cross-sectional STEM/TEM foils in this study were prepared using FEI Scios dualbeam focused ion beam (FIB) equipped with a Ga-ion source.

Indentation hardness measurements were conducted on the five Nb/Mg nanocomposites to determine the effect of layer thickness on strength (hardness). The hardness measurements were conducted using a diamond Berkovich tip using two nanoindentation machines - the Hysitron TriboindenterTM and the KLA XPTM. A total of 50 tests per sample were performed in each instrument using a 10 s (loading) – 100 s (hold) – 10 s (unloading) cycle. Tests were done to a maximum displacement of 200 nm for the Hysitron TriboindenterTM (instrument limit) and up to a maximum displacement of 200 and 400 nm for the KLA XPTM. These choices of indentation depth were chosen to ensure that in each case, the indenter was sampling regions beyond at least one bilayer thickness (2h).

To compare the uniaxial deformation response across these samples, micropillar compression experiments were carried out on all five sets of Nb/Mg nanocomposites with the compression axis normal to the Nb/Mg interface planes (isostress orientation). The

Table 1Summary of TEM/STEM investigations.

Individual Nb and Mg layers average thickness measured using STEM (nm)	Observed phases	Observed local thickness variation of bcc and hcp phases of Mg	Growth direction	Structural orientation relationships observed in between the substrate, Nb and Mg layers
1.7 ± 0.12 nm (Nb)/	Nb: bcc	Close to substrate:	[101] _{Nb,Mg}	[110] _{Si} [111] _{Nb} [111] _{Mg}
1.9 ± 0.16 nm (Mg) 5.5 nm (Nb)/ 5.5 nm (Mg)	Mg: bcc Nb: bcc Mg: bcc	Entirely bcc: 1.5 nm - 2.1 nm See Ref [20,24] for details. Not measured in this work.	$[\bar{1}01]_{\mathrm{Nb},\mathrm{Mg}}$	$(001)_{Si} \parallel (\bar{1}01)_{Nb} \parallel (\bar{1}01)_{Mg}$ $[110]_{Si} \parallel [111]_{Nb} \parallel [111]_{Mg}$ $(001)_{Si} \parallel (\bar{1}01)_{Nb} \parallel (\bar{1}01)_{Mg}$
$8.4 \pm 0.82 \text{ nm (Nb)}/$	Nb: bcc	Close to substrate:	$[\bar{1}01]_{\mathrm{Nb},\mathrm{Mg}}$	[110] _{Si} [111] _{Nb} [111] _{Mg}
7.6 ± 0.25 nm (Mg)	Mg: bcc, hcp	Entirely bcc: 7.8 to 8.1 nm. Middle of film: Mixture of bcc and hcp in a single layer: 4.2 nm to 8.1 nm. Towards top of film: Entire layer bcc: 2 nm to 4 nm. Entire layer hcp: 7 nm - 8.5 nm	[0001] _{Nb,Mg}	[1120] _{Mg} (001) _{Si} (101) _{Nb} (101) _{Mg} (0001) _{Mg}
$14.1 \pm 0.11 \text{ nm (Nb)/}$ $18.9 \pm 0.18 \text{ nm (Mg)}$	Nb: bcc Mg: bcc, hcp	Mg layer thickness at the Nb/Mg interface closer to the substrate (Mg bottom interface): bcc: a few monolayers to 1 nm. At the Mg/Nb interface farther away from the substrate (Mg top interface): bcc: 0.5 nm - 2 nm. hcp Mg: 17 nm - 21 nm	[101] _{Nb,Mg} [0001] _{Nb,Mg}	$ \begin{array}{c} [110]_{Si} \mid\mid [111]_{Nb} \mid\mid [111]_{Mg} \\ \mid\mid [11\bar{2}0]_{Mg} \\ (001)_{Si} \mid\mid (\bar{1}01)_{Nb} \mid\mid (\bar{1}01)_{Mg} \\ \mid\mid (0001)_{Mg} \end{array} $
$76.6 \pm 0.17 \text{ nm (Nb)/}$ $62.6 \pm 0.26 \text{ nm (Mg)}$	Nb: bcc Mg: bcc, hcp	Bcc Mg layer thickness at the Nb/Mg interface closer to the substrate (Mg bottom interface): a few monolayers to 1 nm. At the Mg/Nb interface farther away from the substrate (Mg top interface): bcc: 0.5 nm - 4 nm. hcp Mg: 60 nm - 65 nm	[101] _{Nb,Mg} [0001] _{Nb,Mg}	$ \begin{array}{c} [110]_{Si} \mid\mid [111]_{Nb} \mid\mid [111]_{Mg} \\ \mid\mid [11\bar{2}0]_{Mg} \\ (001)_{Si} \mid\mid (\bar{1}01)_{Nb} \mid\mid (\bar{1}01)_{Mg} \\ \mid\mid (0001)_{Mg} \end{array} $

Terminology. There are two Nb/Mg interfaces which have been named with respect to the growth direction.

Bottom interface: Nb/Mg interface at the bottom of the Mg layer. This interface forms earlier, and is closer to the substrate.

Top interface: Mg/Nb interface at the top of the Mg layer. This interface forms later, and is away from the substrate.

micropillars were fabricated using dual-beam FEI HeliosTM and FEI SciosTM FIB-SEMs, using a beam of Ga⁺ ions to remove the material and shape it in pillar form. Micro-pillars with circular crosssection were fabricated on all five Nb/Mg layer thicknesses. The circular micro-pillars had a height-to-diameter ratio of around 2:1 $(5 \mu m: 2.5 \mu m)$ and around six degrees of vertical taper for all but the smallest Nb/Mg layer thickness. Since the total film thickness of the smallest Nb/Mg 1.7 nm/1.9 nm layer was only \sim 1.6 μ m, a 1:1 height-to-diameter ratio micropillar was fabricated for this case. The pillar dimensions were specifically chosen to be significantly larger than the individual layer thicknesses, as well as to be large enough so that the effects of any FIB induced damage can be minimized. Earlier experimental [35] and computational [36] studies have suggested that the effect of any FIB-altered microstructure on micropillar plasticity is negligible for pillar diameters larger than 1 μm. All the micropillars described in this work are well above this critical size. Additional tests were also conducted on the larger layer thicknesses where the pillar diameters were varied in the range of 1.5 to 5 μm; no appreciable difference in the mechanical properties were observed from these tests. Due to the taper, the diameter measured at the pillar top (the smallest measurement) was used for stress calculations. To gage repeatability, 3-5 micropillars of each layer thickness were tested in micro-compression.

We also examined the effect of pillar cross-section shape (circular vs. square) on the overall mechanical response in the micro-compression experiments of these Nb/Mg multilayered nanocomposites. Micro-pillars of circular cross-section often have an unavoidable taper (in the order of 3–6°) along their height which results in higher stresses at the top of the pillar, whereas square pillars can be fabricated without any taper (by milling each side of the pillar separately with slight over-or-under tilting). However, some studies have speculated that the sharper lateral edges of the square pillar geometry could generate stress concentrations and thus adversely affect the mechanical response, as compared to

circular pillars where the stresses are more uniformly distributed. The effects of these stress distributions are expected to vary depending on the material system [37]. In order to study these factors systematically for our nanocomposites that have much higher strengths and lower strain to failures than softer monolithic Cu specimens studied previously [37], we fabricated and tested micropillars of square cross-section with similar cross-sectional areas and pillar volumes as the circular pillars. Two height-to-width ratios were chosen for this comparative study: square micro-pillars of 2:1 height-to-width ratio were fabricated for the 8.4 nm/7.6 nm Nb/Mg layer thickness nanocomposite, while a 1:1 height-to-width ratio was chosen for the square micropillars fabricated on the 1.7 nm/1.9 nm Nb/Mg layer thickness sample. Similar to the circular pillars, 3-5 micropillars for each layer thickness were tested to ensure repeatability of the data.

The micro-compression experiments were conducted using two nanomechanical testing instruments the Hysitron PI-85TM and the Alemnis SEM indenter. Tests were performed *in-situ* inside of scanning electron microscopes (SEMs, FEI Scios, Helios and MagellanTM) in order to capture the local microstructural evolution during deformation. The pillars were compressed with flat punch conductive diamond tips of 5 and 20 μ m diameters, at a nominal displacement rate of 2 nm s⁻¹. The continuously captured image scans were recorded as a video file during the test. The strain measurements during micropillar compression testing were corrected for compliance following the procedures described in [20].

3. Results

3.1. TEM analysis of Nb/Mg nanolaminates

Table 1 and Figs. 1–4 summarize the relevant microstructural features observed using TEM/STEM, such as the measured individual layer thicknesses, the phases and interface crystallography, for

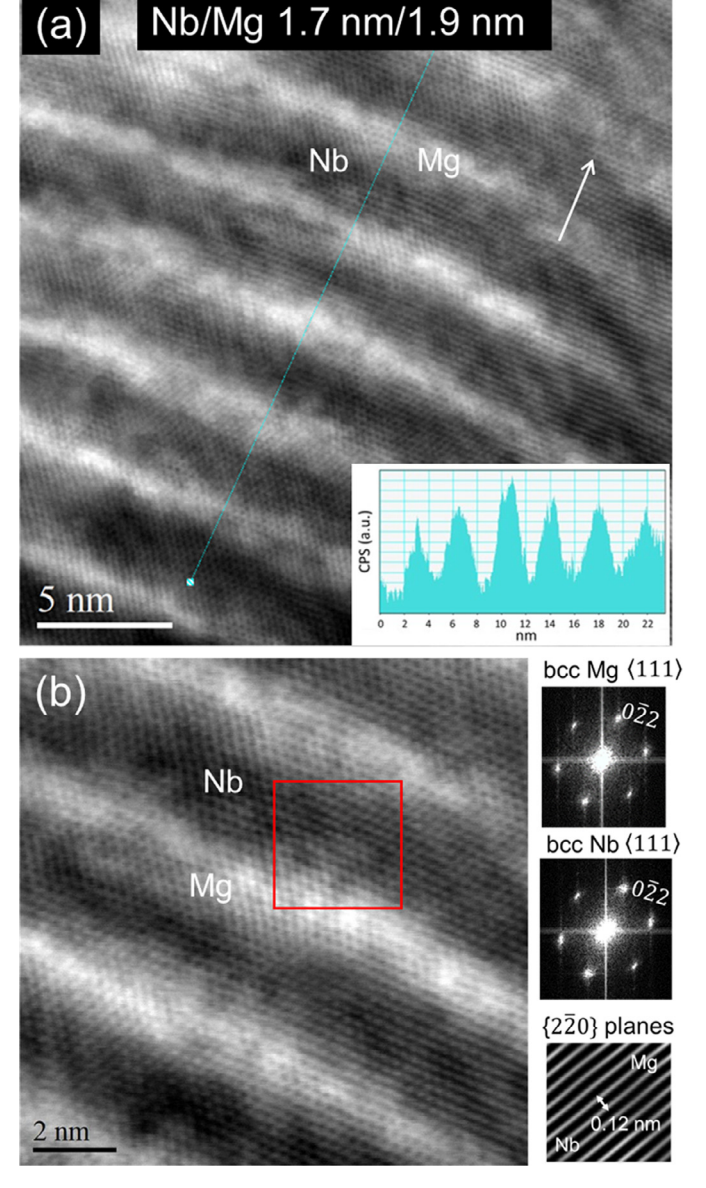


Fig. 1. (a) A bright-field HR-STEM image of the Nb/Mg multilayer with layer thickness of 1.7 nm/1.9 nm along with the thickness fringe profile. The bright and dark regions in the micrograph represent Mg and Nb layers respectively. The white arrow indicates the growth direction of the film i.e., along the [110]. (b) HR-STEM image along with the FFT patterns acquired in Mg and Nb regions of the same sample. A Fourier filtered image for the region enclosed by a red-colored box shows the coherent interface between Nb and Mg {20} lattice planes.

all five as-deposited Nb/Mg nanocomposites in the order of increasing layer thickness. As seen from Table 1, our TEM analysis reveals that Mg is present in its pseudomorphic bcc structure for the two smaller Nb/Mg layer thicknesses of 1.7 nm/1.9 nm and 5.5 nm/5.5 nm (see also Fig. 1). In contrast, in the two largest Nb/Mg layer thicknesses (14.1 nm/18.9 nm and 76.6 nm/62.6 nm), a thin layer of bcc Mg is present at the Nb/Mg interface followed by hcp Mg. The thickness of this thin bcc Mg layer at the Nb/Mg interface varies depending on the growth direction. The bcc Mg layer was measured to be a few atomic planes up to 1 nm thick at the bottom of each individual Mg layer (i.e., at the Nb/Mg interface closer to the substrate), while the bcc Mg layer thickness was slightly but consistently larger – from a few atomic planes up to 4 nm thick – at the top of each individual Mg layer (i.e., at the Mg/Nb interface farther away from the substrate). These observa-

tions will be further discussed in detail later in Figs. 3 and 4. The intermediate thickness Nb/Mg 8.4 nm/7.6 nm nanolaminate was found to have a mix of both bcc and hcp Mg phases, and the bcc vs. hcp Mg phases were found to vary along the thin film height (Fig. 2). Thus, closer to the substrate the Mg layer was present in its pseudomorphic bcc structure (similar to what was observed for the two smaller Nb/Mg layer thicknesses of 1.7 nm/1.9 nm and 5.5 nm/5.5 nm). Towards the middle of the thin film height a mix of both bcc and hcp phases were found, while towards the top of the thin film some Mg layers were observed which were entirely in the hcp phase (without any thin bcc Mg layers). As such, for the three larger layer thicknesses studied in this work -8.4 nm (Nb)/7.6 nm (Mg), 14.1 nm (Nb)/18.9 nm (Mg) and 76.6 nm (Nb)/62.6 nm (Mg) - the volume fraction of bcc Mg was found to decrease with increasing Nb/Mg layer thickness. In other words, the volume fraction of bcc Mg is largest in the 8.4 nm/7.6 nm Nb/Mg multilayer and smallest in the 76.6 nm/62.6 nm Nb/Mg multilayer.

Fig. 1a shows the bright-field STEM micrographs of the Nb/Mg multilayer with layer thickness of 1.7 nm/1.9 nm. In these images, the bright contrast regions correspond to Mg and the dark contrast regions correspond to Nb, which can be used to identify the deposited layers as well as their thicknesses. The corresponding thickness measurement profiles across these images are shown in Fig. 1a **inset**, and the extracted average individual layer thicknesses for the Nb/Mg nanolaminates are found to be 1.7 nm (Nb)/1.9 nm (Mg) (Table 1). The FFT patterns acquired from different regions of the nanolaminate are displayed in Fig. 1b. The identical FFT patterns for Nb and Mg confirm that Mg was deposited in a bcc structure along the (111) orientation. Furthermore, the Fourier filtered image shown in Fig. 2b reveals the coherent nature of the interface between Mg and Nb layers, indicating the pseudomorphic growth of bcc Mg on top of bcc Nb, and the extracted lattice constant of Mg is 0.3394±0.005 nm which coincides well with the lattice constant of Nb (0.33 nm). It should be noted that the bcc Mg in this work is strained to the lattice constant of bcc Nb. As a result, the FFT patterns for bcc Mg and bcc Nb are identical for the (111) orientation.

The microstructural results for the Nb/Mg multilayered nanocomposite with layer thickness of 5.5 nm/5.5 nm are similar to those shown in Fig. 1 (see also Table 1) and are not repeated here. The Nb/Mg 5.5 nm/5.5 nm layer thickness sample has been described in detailed in our previous reports [20,24], wherein synchrotron X-ray diffraction analysis showed that the Mg phase not only entirely transforms to bcc, but also adopts the lattice parameter of Nb (a=3.305 Å) [24]. It is relevant to point out that our results for the Nb/Mg 5.5 nm/5.5 nm layer thickness sample are different from those of prior works by others of similar (\sim 5 nm) Mg layer thicknesses [21]. In those reports the structure of the Mg phase was described to be only partially transformed to bcc in the multilayer.

In contrast, the 8.4 nm/7.6 nm Nb/Mg multilayered nanocomposite shown in Fig. 2 exhibits signatures of both bcc Mg and hcp Mg phases. The bright-field STEM image along with the thickness fringe profile shown in Fig. 2a show the average thicknesses of the Nb and Mg layers to be 8.4 \pm 0.82 nm and 7.6 \pm 0.25 nm respectively (see also Table 1). The high-resolution TEM image shown Fig. 2b was acquired from a region close to the substrate (i.e., towards the bottom section of the film). As confirmed by the FFT patterns "1", "2" and "3", the Mg (bright) layers are found to exist in a bcc phase. These FFT patterns are consistent with the $\langle 111 \rangle$ orientation of bcc phase of Mg. In contrast, the Mg layers shown in Fig. 2c (which was acquired from a region close to the midsection of the film) consists of regions of both bcc and hcp Mg phases as indicated by the corresponding FFT patterns along the $\langle 111 \rangle$ and $\langle 11\bar{2}0 \rangle$ orientations. Further up towards the top of the film, the

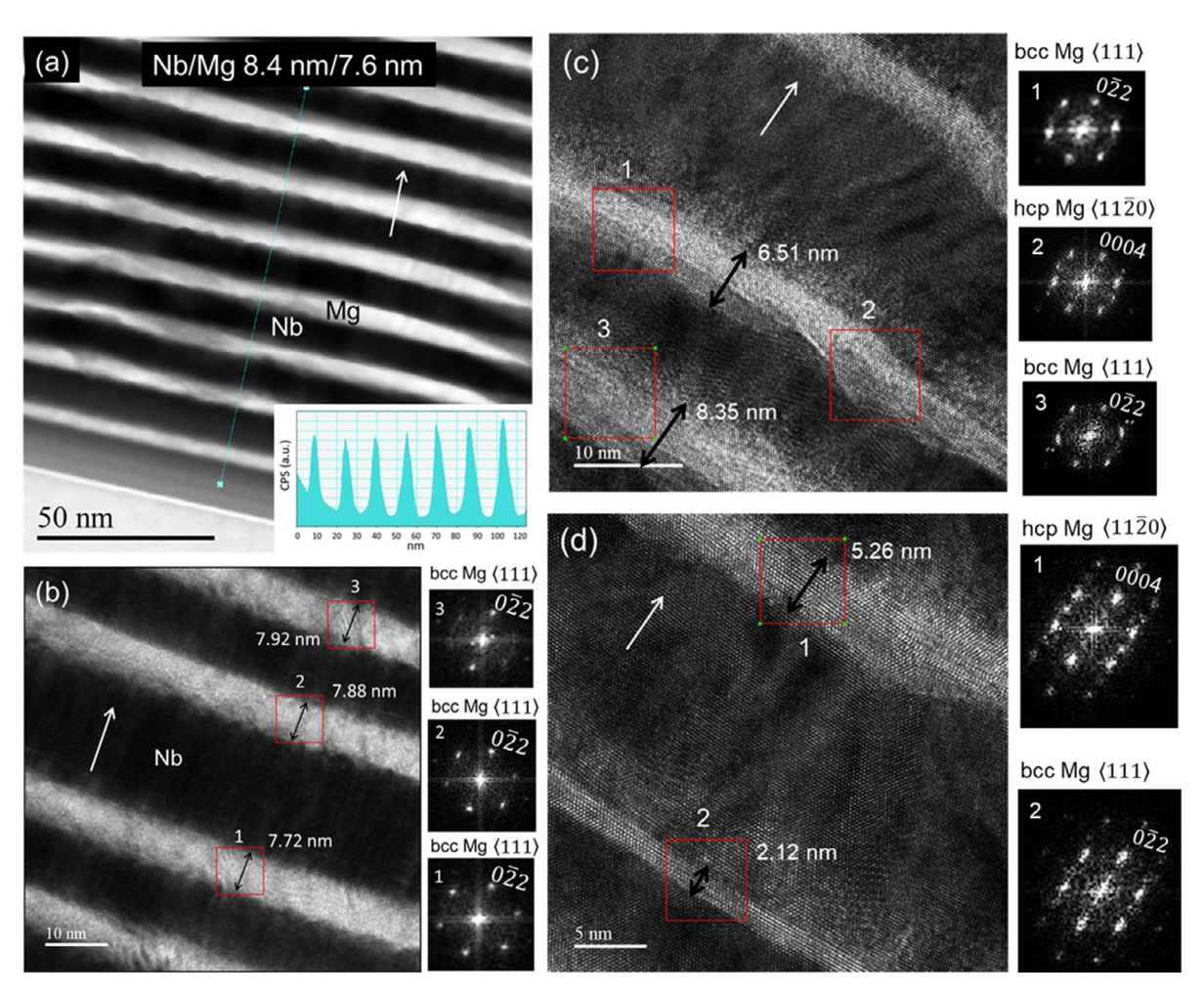


Fig. 2. (a) A bright-field HR-STEM image of the Nb/Mg multilayer with layer thickness of 8.4 nm/7.6 nm along with the thickness fringe profile. (b) HR-TEM image close to the substrate/film interface along with the corresponding FFT patterns acquired in the different regions shown by the red-colored boxes of the Nb/Mg multilayer. The FFT patterns confirm the bcc phase of Mg along the (111) orientation. (c) shows an HR-TEM image of Mg and Nb layers close to the midsection of the film where the FFT patterns '1' and '2' confirm that the Mg layer has regions where the layer is entirely bcc and entirely hcp respectively, whereas the FFT pattern '3' confirms the bcc phase of Mg along the (111) orientation, and (d) shows the structure of two bright Mg layers separated by a dark Nb layer towards the top of the thin Mg/Nb film, where the top Mg layer is consistent with the (1120) of hcp Mg and the bottom Mg layer is consistent with the (1111) orientation of bcc Mg. The white arrows in the various images show the PVD growth direction of the Nb/Mg multilayer.

high-resolution image along with the FFT patterns in Fig. 2d show that locally individual Mg layers can be entirely bcc or entirely hcp. The FFT pattern labeled as '1' in Fig. 2d is consistent with the $\langle 11\bar{2}0 \rangle$ orientation of hcp Mg, whereas the FFT pattern labeled as '2' is consistent with the $\langle 111 \rangle$ orientation of bcc Mg.

Thus, the results from Fig. 2 indicate that the individual Mg layers are entirely bcc close to the substrate, and as we move away from the substrate along the growth direction the individual Mg layers can exist in either their bcc and/or hcp forms. Further detailed TEM investigations reveal that the local bcc Mg layer thickness in this nanolaminate is non-uniform and can vary from approximately 2 nm to 8.1 nm in this multilayer, whereas the local thicknesses of the layers where Mg is entirely hcp vary from 7 to 8.5 nm (see Table 1). These thicknesses are much larger than the 4.2 nm layer thickness predicted for a pseudomorphic hcp-tobcc phase transformation in Mg using DFT calculations [23]. Our results suggest that the pseudomorphic hcp-to-bcc phase transformation in Mg is strongly dependent on the thin film stresses present during deposition. The individual layer thicknesses in the Nb/Mg 8.4 nm/7.6 nm multilayered nanocomposite are close to the hcp-to-bcc phase transformation of Mg, and hence even a relatively small variation in the local stress state in the film affects the Mg phase transformation. The variability of the local stress environment can be seen by comparing Figs. 2a vs. 4a. These figures show the typical evolution of the interface morphology in PVD depositions. Thus, the deposited layers are flat close to the substrate (Fig. 2a) but fluctuations in the deposition conditions and the resultant shadowing and curtaining effects cause the layers to become wavy with increasing film thickness and also show varying layer thicknesses. As the waviness in the layers increase, the highly crenulated regions are expected to have a very different local stress state which can affect the hcp-to-bcc phase transformation in Mg (Fig. 4a) [38,39].

Figs. 3 and 4 show the structure of the Nb and Mg Nb layers along with the thickness fringe profiles for the two larger Nb/Mg layer thicknesses of 14.1 nm/18.9 nm (Fig. 3a) and 76.6 nm/62.6 nm (Fig. 4a) respectively. The FFT pattern obtained from the whole image of Fig. 3a contains spots corresponding to bcc Nb and hcp Mg, where spots of (111) bcc Nb and (11 $\bar{2}0$) hcp Mg overlap, and the 10 $\bar{1}0$ type reflection of hcp Mg is also present. This observation confirms that Mg is deposited in hcp form for the Nb/Mg 14.1 nm/18.9 nm multilayer. However, a careful examination of the Nb/Mg interface in this multilayer reveals the presence of a thin layer of bcc Mg at the bottom of each individual Mg layer (i.e., at the Nb/Mg interface closer to the substrate with respect to the growth direction), as shown in Fig. 3c. A similar thin layer of

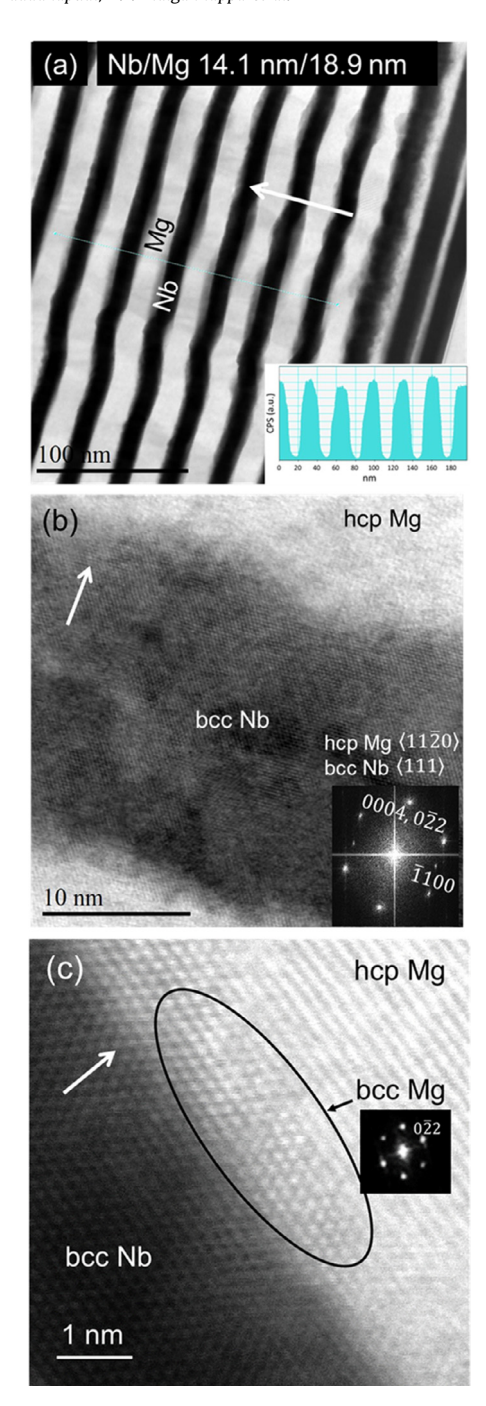


Fig. 3. (a) A bright-field HR-STEM image of the Nb/Mg multilayer with layer thickness of 14.1 nm/18.9 nm along with the thickness fringe profile, (b) HR-STEM image along with the FFT pattern obtained from the whole image, shows the $\langle 11\bar{2}0\rangle$ of hcp Mg, where the 0004 reflection overlaps with the 2 $\bar{2}0$ reflection of bcc Mg along the $\langle 111\rangle$ orientation, and (c) shows the presence of a thin layer of bcc Mg at the Nb/hcp Mg interface (i.e., at the Nb/Mg interface closer to the substrate). The black ellipse in (c) highlights the bcc phase of Mg and the corresponding FFT pattern obtained at the Nb/Mg interface is also displayed. The white arrows in images indicate the PVD growth direction of the Nb/Mg multilayer.

bcc Mg was also present at the top of each individual Mg layer (i.e.,at the Mg/Nb interface farther away from the substrate). The thicknesses of these bcc Mg layers were found to be non-uniform between the bottom and top Nb/Mg interfaces, and it varies from a few atomic planes to 1 nm thick for the Nb/Mg interface closer to the substrate (Fig. 3c) and from a few atomic planes to 2 nm

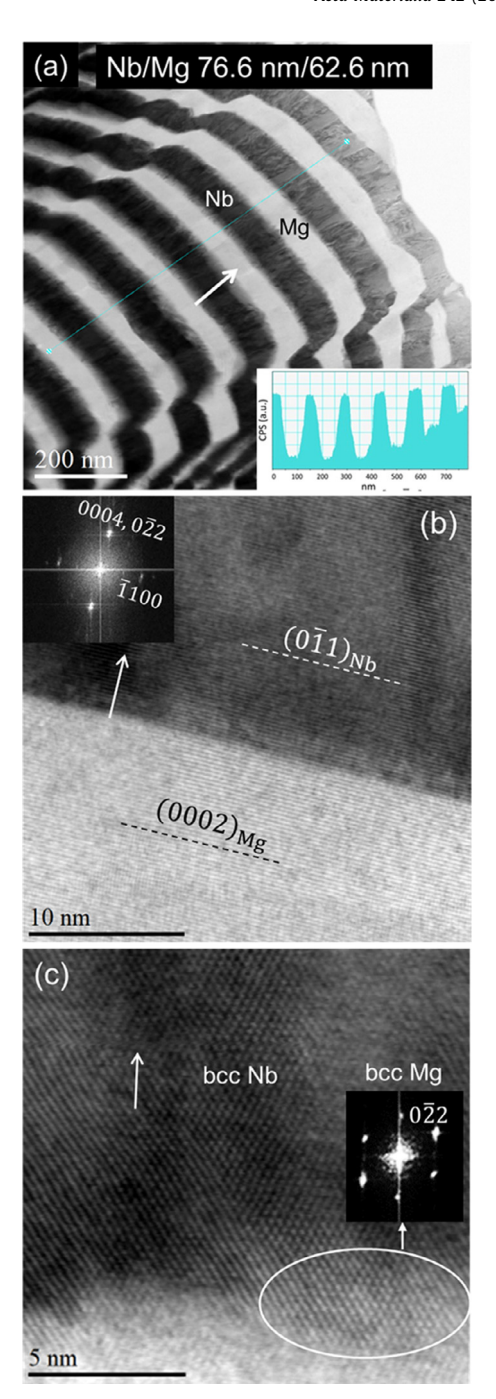


Fig. 4. (a) A bright-field HR-STEM image of the Nb/Mg multilayer with layer thickness of 76.6 nm/62.6 nm along with the thickness fringe profile, (b) HR-STEM image along with the FFT pattern acquired from the whole image of the same sample, shows the $\langle 1120 \rangle$ of hcp Mg, where the 0004 reflection overlaps with the 220 reflection of bcc Mg along the $\langle 111 \rangle$ orientation, and the region circled in white color in (c) shows the bcc Mg phase at the interface of hcp Mg/Nb (i.e., at the Mg/Nb interface farther away to the substrate with respect to the growth direction). The FFT pattern of bcc Mg is consistent with the $\langle 111 \rangle$ orientation of bcc phase. The white arrows in the images represent the PVD growth direction of the Nb/Mg multilayer.

thick for the Mg/Nb interface farther away from the substrate (see Fig. 4c for the Nb/Mg 76.6 nm/62.6 nm layer thickness).

A similar high-resolution TEM analysis confirms the presence of hcp Mg and bcc Mg for the 76.6 nm/62.6 nm Nb/Mg layer thickness in Figs. 4b and 4c. The thickness of bcc Mg region at the Nb/Mg interface is again found to be non-uniform and it varies from few atomic planes up to 1 nm thick at the bottom of each

Table 2Comparison between micropillar compression and indentation hardness response of Nb/Mg nanocomposites of varying layer thicknesses in terms of average and standard deviation taken over at least 3 tests. The effect of pillar cross-section shape (circular vs. square) on the uniaxial mechanical response has also been indicated. The values of stress and strain at instability without any standard deviation refer to a single test taken to failure.

Mg/Nblayer thickness	Hardness(H) (GPa)	Pillarcross-section shape	0.2% off set Yield Stress (GPa)	<u>н</u> Yield	Stress at instability (GPa)	Strain at instability
Nb/Mg(bcc) 1.7 nm/1.9nm	4.8 ± 0.34	Circular	2.03±0.02	2.36	2.79	0.11
		Square	2.02 ± 0.02	2.38	2.74	0.10
Nb/Mg(bcc) 5.5 nm/5.5nm	3.7 ± 0.26	Circular	1.41 ± 0.01	2.62	2.7 ± 0.11	0.14 ± 0.009
Nb/Mg(bcc+hcp) 8.4 nm/7.6nm	3.2 ± 0.22	Circular	1.38 ± 0.09	2.32	2.30	0.08
		Square	1.35 ± 0.10	2.37	2.26	0.07
Nb/Mg(hcp)	2.4 ± 0.36	Circular	1.28 ± 0.03	1.88	$1.94{\pm}0.05$	0.07 ± 0.005
14.1 nm/18.9 nm						
Nb/Mg(hcp)	2.0 ± 0.32	Circular	$1.24{\pm}0.05$	1.61	$1.80 {\pm} 0.04$	0.06 ± 0.008
76.6 nm/62.6 nm						

individual Mg layer (i.e. at the Nb/Mg interface closer to the substrate, see Fig. 3c for the Nb/Mg 14.1 nm/18.9 nm layer thickness) to a few atomic planes up to 4 nm thick at the top of each individual Mg layer (i.e. at the Mg/Nb interface farther away from the substrate, Fig. 4c). For both the Nb/Mg 14.1 nm/18.9 nm and 76.6 nm/62.6 nm layer thicknesses the bcc Mg layer at the interface was found to be consistently thicker at the Mg/Nb interface farther away from the substrate. A similar observation was also reported in [21], where the authors had observed a thin distorted layer (~1 nm) of bcc Mg at the Mg/Nb interface.

3.2. Effect of layer thickness and crystal structure: micromechanical investigations

Before investigating the layer phase and size effects on Nb/Mg nanolaminate strength, we first examine the effect of micro-pillar cross-section shape on the mechanical response. Fig. 5 shows the engineering stress-strain curves obtained from micro-compression experiments on pillars of square vs. circular cross-sectional geometries for the Nb/Mg layer thicknesses of 1.7 nm/1.9 nm and 8.4 nm/7.6 nm. The relevant plastic properties, such as 0.2% offset yield stress, and stress and strain at instability in these pillars are summarized in Table 2. Note that while the micro-pillars for the larger Nb/Mg 8.4 nm/7.6 nm layer thickness were fabricated to have a height-to-diameter ratio of around 2:1 (5 µm:2.5 µm), the micro-pillars on the smaller thickness Nb/Mg 1.7 nm/1.9 nm nanolaminate only had a 1:1 height-to-diameter ratio in order accommodate the smaller film thickness (\sim 1.6 μ m) in this nanolaminate. However in either case, the pillar dimensions are significantly larger than the nm-level individual layer thicknesses of the nanolaminate systems being studied. Hence the deformation response in the pillars are expected to be dominated by the layer thicknesses present in the nanolaminate films, and not the pillar aspect ratios. Other studies [40] have also reported the effect of pillar aspect ratios to be negligible when studying multilayered nanocomposite systems with layer thicknesses in the nanometer

As seen from Fig. 5 and Table 2, similar mechanical responses – such as 0.2% offset yield stress values, stress at instability, strain at instability, as well as the general in-situ deformation behavior (see videos S1 through S6 in Supporting documents) and post-deformation images of the micro-pillars – were observed in both square vs. circular pillar shapes for the two Nb/Mg layer thicknesses. There is a slight difference at the point of instability and in the post-instability region between the square vs. circular pillars in the case of the Nb/Mg 8.4 nm/7.6 nm layer thickness (see Fig. 5B). However, at and beyond the point of instability the pillar deformation is no longer uniaxial, and hence the mechanical data beyond this point (denoted by the dashed lines) are of little value to the aim and conclusions of this study. Hereinafter we focus on

the results obtained primarily from the circular cross-section pillars.

The foregoing results are consistent with previous work on square vs. circular micro-pillar geometries of Cu (100) on MgO substrate performed by Kiener et al. [37]. Similar to the results shown in Fig. 5, these authors also did not observe any significant difference between rectangular and cylindrical micro-pillar geometries was observed for Cu (100) on MgO. However, the threedimensional finite element (FE) modeling employed in their work suggested that the side edges present in the square micro-pillar geometry can give rise to slight stress inhomogeneities due to excessive stress concentrations developing at these edges. The overall effect of such stress inhomogeneities on the mechanical properties of the micro-pillars was found to be negligible. While there may be a material influence on the pillar shape effect (i.e., Cu (100) on MgO substrate in [37] vs. Nb/Mg multilayers on Si in this work), this observation provides an explanation for the minor discrepancies noted in the post-instability regions between the circular and square pillars for the Nb/Mg 8.4 nm/7.6 nm layer thickness (Fig. 5B).

Our results along with the other reports from literature [37] suggest that either the square or the circular micro-pillar geometries can be used to reliably examine the micro-compression response in nanolaminates. This is an important advantage, since square pillars can be fabricated with minimal taper by ion-milling each side of the pillar separately with slight over-or-under tilting in order to reduce tapering. Thus, four-sided micro-pillars of square cross-sectional shape can be recommended for use in cases where the pillar tapering is a concern. Moreover, micro-pillars of square cross-sectional shapes are often the only option in certain loading scenarios, such as when compression is applied parallel or oblique to the interface planes, as was performed for Nb/Mg nanolaminates in [41]. Fig. 5 demonstrate that the results from square pillars can be treated similarly to those of other circular pillars reported in the literature.

Fig. 6 (see also the summary in Table 2) presents the representative engineering stress-strain curves obtained from microcompression experiments on (circular) pillars for all five Nb/Mg multilayer nanocomposites classified by their layer thicknesses. A notable observation from Fig. 6 is that the deformation response of the nanolaminates can be divided into two broad categories. For the two larger Nb/Mg 14.1 nm/18.9 nm and 76.6 nm/62.6 nm layer thicknesses, an instability is observed at or near the peak compressive strength which is followed by inhomogeneous deformation in multiple localized regions throughout the pillar. This behavior is similar to that of most hcp materials when compressed along their c-axis [42]. In both of our two larger Nb/Mg 14.1 nm/18.9 nm and 76.6 nm/62.6 nm layer thicknesses, the c-axis of the hcp Mg layer is parallel to the loading axis (see Table 1). Hence the deformation behavior in these two layer thicknesses is expected to be dom-

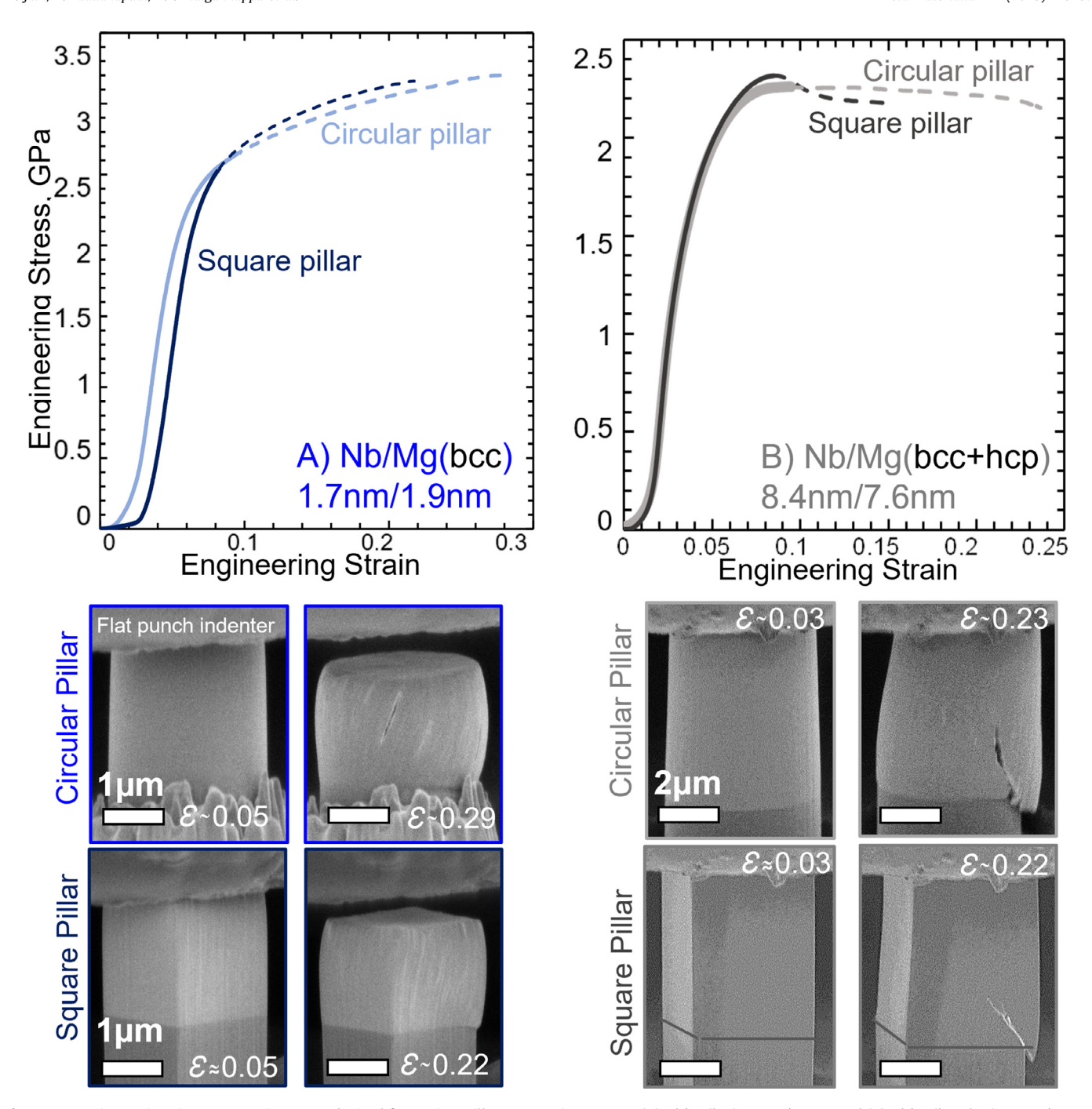


Fig. 5. Comparing engineering stress-strain curves obtained from micro-pillar compression tests on (A) Nb/Mg(bcc) 1.7 nm/1.9 nm and (B) Nb/Mg(bcc+hcp) 8.4 nm/7.6 nm on two pillar cross-section shapes (Square vs. Circular) and the corresponding SEM images after deformation.

inated by the response of the hcp Mg in the nanolaminates. In contrast, the applied strain is accommodated more homogeneously in the three smaller Nb/Mg layer thicknesses (1.7 nm/1.9 nm, 5.5 nm/5.5 nm, and 8.4 nm/7.6 nm). Such behavior is reminiscent of other bcc nano-structured metals, like steel, Ta, and Fe, which behave similarly in micro pillar compression and maintain a high flow stress over an extended straining region [43]. In our work, Mg is entirely in its pseudomorphic bcc structure in the two smallest Nb/Mg layer thicknesses (1.7 nm/1.9 nm and 5.5 nm/5.5 nm), while the volume fraction of bcc Mg is also considerably large in the intermediate thicknesses 8.4 nm/7.6 nm Nb/Mg multilayer (see Table 1). Thus, the deformation behavior in these three smaller layer thicknesses is thought to be dominated by the response of the pseudomorphic bcc Mg in the nanolaminates.

Fig. 6 and Table 2 also show that significant increases in strength as the individual layer thicknesses of the Nb and Mg layers are reduced from 76.6 nm/62.6 nm to 1.7 nm/1.9 nm. The strength values are replotted in Fig. 7 which depicts the 0.2% offset yield strength values from the micro-compression experiments (Fig. 7a) along with the indentation hardness values (Fig. 7b) as a function of the bi-layer thicknesses (2 h) for each Nb/Mg nanocomposite on a Hall-Petch type of plot.

Somewhat different trends are observed in the micro-compression vs. indentation measurements. The 0.2% offset yield strength values from the micro-compression experiments show a distinctly different strength scaling for the two larger Nb/Mg layer thicknesses whose deformation response is hcp-Mg dominated vs. the three smaller Nb/Mg layer thicknesses where the pesudomor-

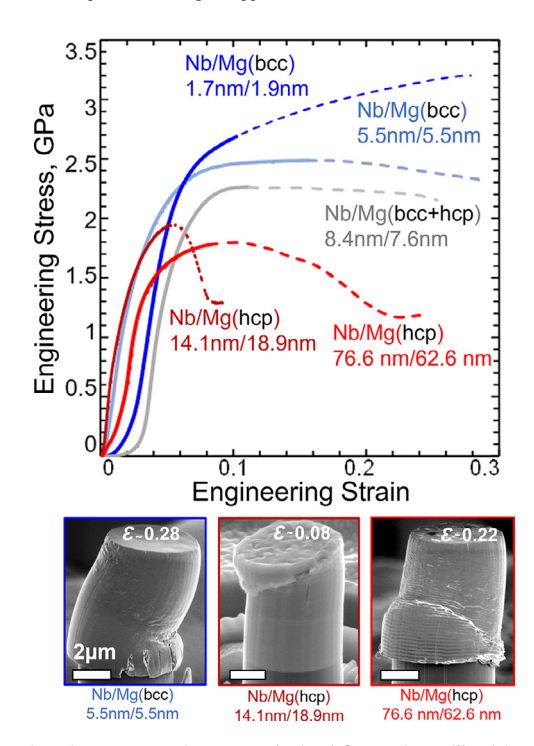


Fig. 6. Engineering stress-strain curves obtained from micro-pillar (circular) compression tests on five different layer thicknesses of Nb/Mg in normal orientation (loading axis normal to the interfaces). Images of deformed pillars of Nb/Mg 5.5 nm/5.5 nm, 14.1 nm/18.9 nm and 76.6 nm/62.6 nm after compression are shown while Nb/Mg 1.7 nm/1.9 nm and 8.4 nm/7.6 nm are shown in Fig. 5. The instability point in the tests is marked by the end of the solid lines; the dashed lines in the figure indicate that the tests are no longer uniaxial, and thus, the data beyond this level is not reliable.

phic bcc Mg is present (0.45 vs. 2.54 GPa \sqrt{nm} , Fig. 7a). This is a remarkable and highly unusual result since the strength of a nanolaminate is expected to plateau with decreasing layer thicknesses [1]. Instead, here we observe the opposite effect — a renewed strengthening regime enabled by the hcp \rightarrow bcc phase transition in Mg, a point we revisit later in the discussion.

The hardness values of the Nb/Mg nanocomposites are also exceptionally higher, over 10 times that of coarse-grained Mg or Nb, and approximately 2-3 times that the volume average nanocrystalline Mg and Nb [44,45] (Fig. 7b and Table 2). Unlike the uniaxial yield values, the hardness numbers appear to have a similar sensitivity to 2h irrespective of the hcp or bcc nature of Mg in the nanolaminates. Thus, we observe a continuous strengthening effect in the hardness values as 2h decreases, down to 2h = 3.7 nm for the 1.7 nm/1.9 nm Nb/Mg layer thicknesses. The strengthening slope for Nb/(hcp) Mg nanocomposites was calculated to be 6.11 GPa\(\sqrt{nm}\), which is similar to the strengthening slope of 5.67 GPa\/nm in Nb/(bcc) Mg nanocomposites. The strengthening slope considering all five Nb/Mg layer thicknesses is also similar (6.62 GPa\(\sqrt{nm}\)). Our nanoindentation results indicate that by enabling a hcp→bcc phase transition in Mg we are able to increase the strength of the composite to levels that have not been achieved in Nb/Mg nanocomposites before.

These measured strengthening slope values for the Nb/Mg nanocomposites compare favorably to both polycrystalline (non-laminated) Mg, with grain sizes ranging from 4 μ m to 450 μ m, where the Hall Petch slope has been found to vary between $k_y = 1.9$ to 9.3 GPa $\sqrt{\text{nm}}$ [46–50], as well as Mg present in a nanolaminate with reported values of k_y ranging from 4.99 [51] to 10.83 [21] GPa $\sqrt{\text{nm}}$. It is noteworthy to mention that compared to prior results on Nb/Mg PVD films [21] the hardness values for the three smaller bcc-dominated Nb/Mg layer thicknesses

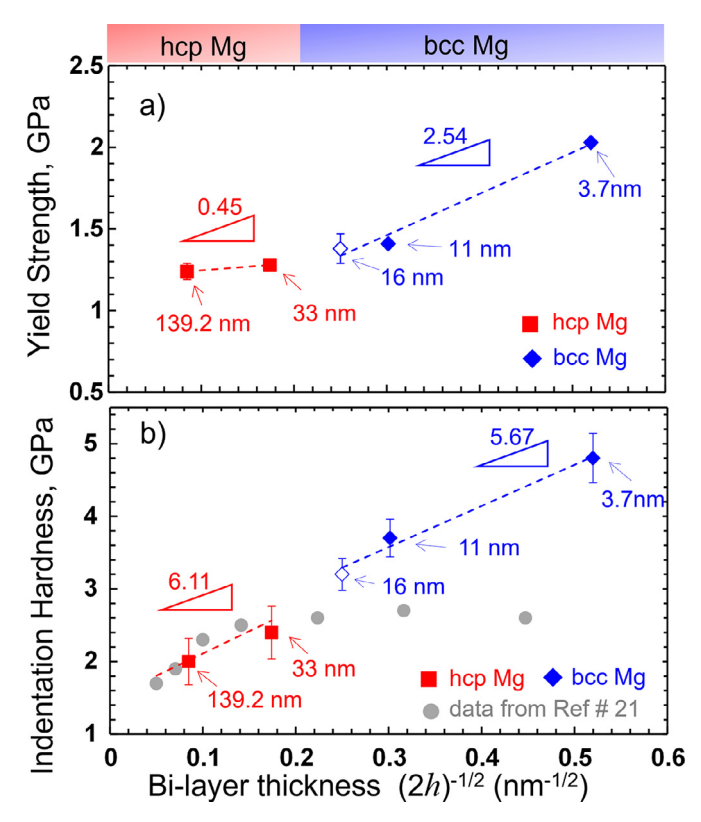


Fig. 7. Hall-Petch plot of (a) 0.2% offset yield strength measured from micro-pillar compression experiments and (b) indentation hardness with bi-layer thickness. The two blue filled diamonds represent bi-layer thicknesses of 3.7 and 11 nanocomposites (Nb/Mg layer thicknesses of 1.7 nm/1.9 nm, and 5.5 nm/5.5 nm respectively), where Mg is present in its pseudomorphic bcc structure. The open blue diamond represents the intermediate thickness Nb/Mg 8.4 nm/7.6 nm nanolaminate (bi-layer thickness 16 nm) which has a mix of both bcc and hcp Mg phases, but the mechanical response of this nanolaminate is dominated by the bcc Mg phase. The filled red square data points represent the 33 and 139.2 nm thick bi-layer composites (Nb/Mg 14.1 nm/18.9 nm and 76.6 nm/62.6 nm layer thicknesses) where the deformation response is dominated by the hcp Mg present in these nanolaminates. Data shown in the gray circles were taken from Ref [21].

(1.7 nm/1.9 nm, 5.5 nm/5.5 nm, and 8.4 nm/7.6 nm) reported in this work are considerably higher (see the data shown in gray circles in Fig. 7b). As mentioned earlier, in [21] the Mg phase in the nanocomposites was not fully bcc Mg until h < 5 nm, which might be the reason for this discrepancy.

A second point of note is that the yield strength vs. hardness strengthening slopes show different trends in our micro-pillar compression vs. nanoindentation results, particularly for the two larger Nb/Mg 14.1 nm/18.9 nm and 76.6 nm/62.6 nm layer thicknesses where Mg is in its hcp phase (Fig. 7a vs. 7b). The strengthening slope of the hardness values (6.11 GPa\sqrt{nm}) is prominently higher in these two nanolaminates than in their yield strength values (0.45 GPa /nm). We suggest that this difference is related to the near uniaxial (micro-pillar compression) vs. multiaxial (nanoindentation) stress states in the deformation zone for these two experimental setups. As mentioned earlier, the PVD deposited hcp Mg layers in these two Nb/Mg multilayers are highly textured (Figs. 3 and 4). Thus, the nominally uniaxial micro-pillar compression experiments are expected to show a strong anisotropy in their deformation response. For example, in the isostress orientation experiments shown in this work (with the compression axis normal to the Nb/Mg interface planes, Figs. 6 and 7a), the loading axis is parallel to the c-axis of the hcp Mg layers in the micro-compression tests. Thus the likely to activate deformation mechanisms in this orientation are hard c-axis pyramidal slip

or contraction twinning. Our previous results have shown that this isostress loading orientation elicits a stronger response compared to other orientations, such as the isostrain orientation where the compression axis is parallel to the Nb/Mg interface planes (1.24±0.05 GPa yield stress for the stronger isostress orientation Fig. 7a and Table 2 vs. 1.02±0.4 GPa for the isostrain orientation for the 76.6 nm/62.6 nm layer thickness [41]). On the other hand, such anisotropy is expected to be less pronounced under the multiaxial loading state present during indentation, since the plasticity during indentation can be accommodated by activating multiple slip modes including the relatively soft basal and prismatic slip modes. A similar difference between nanoindentation and micro-pillar compression has been reported in hcp/hcp Mg/Ti multilayered samples [51], where the shear and tensile stress components under indentation were postulated to activate the soft and easy slip modes in the hcp structures, leading to a strengthening slope ($k_y = 4.99 \text{ GPa}\sqrt{\text{nm}}$ [51]) similar to Fig. 7b. Our results in Fig. 7a vs. 7b suggest that the higher hardening slopes observed under indentation for the larger layer thicknesses would follow a similar trend - i.e., the multiaxial loading state under indentation would allow multiple 'softer' slip systems to be activated in the hcp Mg layers leading to an increased barrier strength along the hcp/bcc interfaces and a higher hardening response.

Another remarkable property is the increased strain to failure with decreasing layer thickness in the Nb/Mg nanocomposites. Fig. 8a and 8b show the stress and strain values at instability respectively as a function of the bi-layer thicknesses (2h) for each Mg/Nb nanocomposite during the micro-pillar compression experiments. The two blue filled diamonds represent bi-layer thicknesses of 3.7 and 11 nanocomposites (Nb/Mg layer thicknesses of 1.7 nm/1.9 nm, and 5.5 nm/5.5 nm respectively), where Mg is present in its pseudomorphic bcc structure. The open blue diamond represents the intermediate thickness Nb/Mg 8.4 nm/7.6 nm nanolaminate (bi-layer thickness 16 nm) which has a mix of both bcc and hcp Mg phases, but the mechanical response of this nanolaminate is dominated by the bcc Mg phase. The filled red square data points represent the 33 and 139.2 nm thick bi-layer composites (Nb/Mg 14.1 nm/18.9 nm and 76.6 nm/62.6 nm layer thicknesses) where the deformation response is dominated by the hcp Mg present in these nanolaminates. We note that only a limited number of pillars were compressed past the failure (instability) stresses in our experiments (see Table 2). However, some trends are apparent even from this limited dataset. The instability stress values in Fig. 8a appear to follow a similar trend to those of the yield stresses in Fig. 7a. Thus, a lower strengthening slope for the two larger hcp-Mg dominated Nb/Mg layer thicknesses is observed, followed by a sharp increase in the strengthening slope up to 2h = 11 nm (5.5 nm/5.5 nm Nb/Mg layer thickness). A plateau in the instability stress is also observed below this layer thickness, and the instability stress for the smallest Nb/Mg layer thickness (1.7 nm/1.9 nm, 2h = 3.7 nm) is virtually identical to that of the 5.5 nm/5.5 nm Nb/Mg layer thickness (\sim 2.7 GPa in both cases, see

The micro-compression strain at instability in the pillars also follows a similar trend. Lower instability strains ($\sim 0.06-0.07$) were measured for the two larger Nb/Mg layer thicknesses whose deformation response is dominated by the hcp-Mg present in the nanolaminates (Nb/Mg 14.1 nm/18.9 nm and 76.6 nm/62.6 nm). The intermediate thickness 8.4 nm/7.6 nm Nb/Mg multilayer also has a similar low instability strain value (0.07–0.08). However, the strain to failure more than doubles (to 0.14 \pm 0.009) for the 5.5 nm/5.5 nm Nb/Mg multilayer where the entire Mg layer is in its pseudomorphic bcc phase. With further decrease in the layer thickness, a slightly lower failure strain (\sim 0.010–0.11) is observed for the smallest 1.7 nm/1.9 nm Nb/Mg layer thickness. Note that even with this decrease, the failure strain for the 1.7 nm/1.9 nm

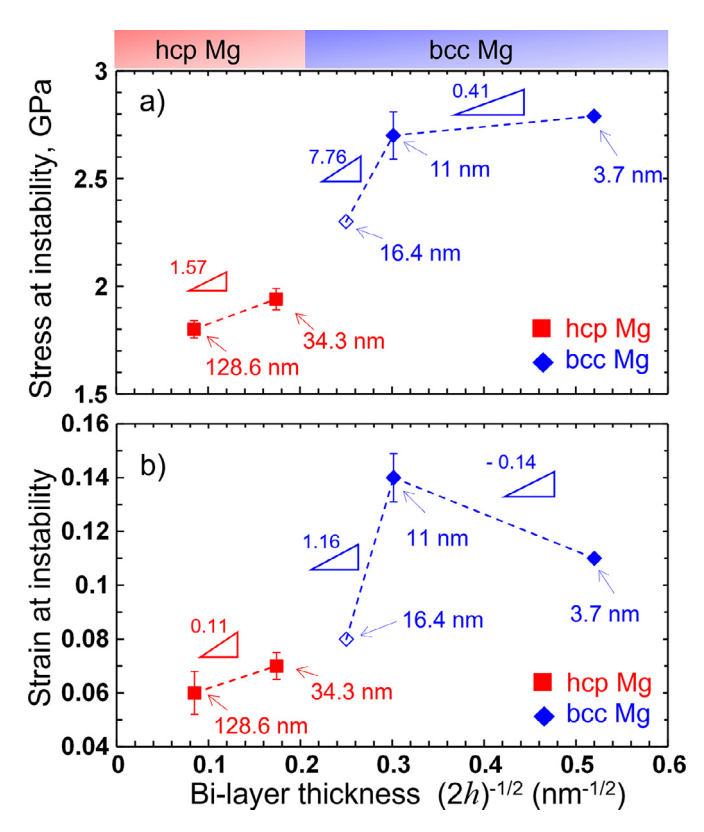


Fig. 8. (a) Stress at instability and (b) strain at instability plotted against the inverse square root of the bi-layer thickness for the five Nb/Mg nanolaminates studied in this work.

The two blue filled diamonds represent bi-layer thicknesses of 3.7 and 11 nanocomposites (Nb/Mg layer thicknesses of 1.7 nm/1.9 nm, and 5.5 nm/5.5 nm respectively), where Mg is present in its pseudomorphic bcc structure. The open blue diamond represents the intermediate thickness Nb/Mg 8.4 nm/7.6 nm nanolaminate (bi-layer thickness 16 nm) which has a mix of both bcc and hcp Mg phases, but the mechanical response of this nanolaminate is dominated by the bcc Mg phase. The filled red square data points represent the 33 and 139.2 nm thick bi-layer composites (Nb/Mg 14.1 nm/18.9 nm and 76.6 nm/62.6 nm layer thicknesses) where the deformation response is dominated by the hcp Mg present in these nanolaminates.

Nb/Mg nanolaminate is 45- 80% higher than the hcp Mg based nanolaminate counterparts (instability strains of $\sim\!0.010\text{--}0.11$ vs. \sim 0.06–0.07).

This is another remarkable result and is in contrast with the conventional trend, where typically the strain to failure decreases with a decrease in layer thickness, crystal diameter or grain size [3,4]. Worthwhile highlighting again is the homogenous deformation behavior of the two smaller Nb/Mg layer thicknesses (1.7 nm/1.9 nm and 5.5 nm/5.5 nm, Fig. 6). These layer thicknesses exhibit uniform deformation until final instability by bending, compared to the localized shear band formation in case of the two larger Nb/Mg 14.1 nm/18.9 nm and 76.6 nm/62.6 nm nanolaminates.

4. Discussion

A key finding of this work is a continued increase *both* in strength (uniaxial and indentation hardness) and in strain to failure with decreasing layer thicknesses, a trend very seldom reported in nanolaminates consisting of pure metals. We suggest two factors that contribute towards such enhanced strength and mechanical stability, namely the change to a coherent interface from an incoherent one (suppresses slip transmission and underlying softening) and introduction of a more plastically isotropic bcc material from an anisotropic hcp structure (promotes co-

deformation). Both these phenomena are achieved by enabling a hcp-to-bcc pseudomorphic phase transition in Mg, resulting in strength and mechanical stability levels that have not been achieved in Mg-based nanocomposites before.

The well known "smaller is stronger" effect has been reported in several metallic nanocrystalline materials [1,52] but there is usually a limit crystal size below which the material strength softens, a so-called inverse Hall-Petch effect. For example, in prior work by Misra et al. on the Cu/Nb multilayer system [1], the plateau (or softening) strength was reported at layer thicknesses below 5-10 nm. It was attributed to a transition from the confined layer slip mechanism, which applies at a few tens of nanometers range, to dislocations starting to transmit across the interface. The TEM analysis of the two smallest thickness Nb/Mg nanocomposites in this work (Nb/Mg 1.7 nm/1.9 nm and 5.5 nm/5.5 nm, where Mg is in its pseudomorphic bcc state, Fig. 1) shows that the interfaces in nanolaminates possess a cube-on-cube orientation relationship and are coherent. Evidently this interface is also resistant to slip transmission as the incoherent one. Further, the coherency stresses and image stresses (due to differences in elastic moduli) could also enhance the resistance to slip transmission.

It is worth highlighting again that the smaller thickness bcc Nb/Mg composites demonstrate an unusually homogeneous response for such fine nanostructured metals (see Fig. 6 for the compression behavior of Nb/Mg 1.7 nm/1.9 nm, 5.5 nm/5.5 nm, and 8.4 nm/7.6 nm). Two factors are expected to contribute to this homogeneous deformation. First, bcc materials have at least 48 slip systems available for deformation with relatively small differences in activation barrier compared to the fewer slip systems in hcp materials. DFT calculations of gamma surfaces have suggested that the same 48 slip systems common to bcc metals are favorable in bcc Mg [23]. Second, the interfaces permit co-deformation of the Mg and Nb nanolayers. This would suggest that plastic deformation in the smaller thickness bcc Nb/Mg multilayers occurs via discrete, single dislocations events. Individual dislocations can nucleate from one boundary and get absorbed at another and do not pile up within the layers. Sustaining homogeneous plasticity relies on the transfer of dislocations across the interfaces to prevent pileups that localize deformation and generate stress concentrations. Further efforts, particularly atomistic simulations or crystal plasticity modeling, may be needed to validate these notions.

The intrinsic structural properties of the bcc Mg phase alone are hard to distinguish from the extrinsic effect of nano-layer confinement and the interface. Prior modeling studies involving density functional theory have indicated that the elastic constants of bcc Mg are higher and more anisotropic than those of hcp Mg [53]. A crystal plasticity model incorporating confined layer slip successfully predicted the deformation response and slip mechanisms underlying the room temperature deformation of bcc/bcc and hcp/bcc Mg/Nb nanolaminates [41]. The modeling work revealed that the bcc Mg phase is stronger than the hcp Mg phase due to not only the reduction in layer thickness but because the glide on the $\{110\}\langle111\rangle$ and $\{112\}\langle111\rangle$ slip systems is harder than basal slip in hcp Mg.

Figs. 2, 3 and 4 also indicate that even for the larger Nb/Mg layer thicknesses there exists a thin layer of the pseudomorphic bcc Mg at the Nb/Mg interface. As mentioned earlier, the thickness of this thin bcc Mg layer is relatively constant across all the three larger Nb/Mg layer thicknesses (Nb/Mg 8.4 nm/7.6 nm, 14.1 nm/18.9 nm and 76.6 nm/62.6 nm) studied in this work. Thus, with increasing overall layer thicknesses the volume fraction of bcc Mg decreases. As seen from the results in Tables 1 and 2, the improvements in strain to failure of the nanolaminates is strongly correlated with the approximate volume fraction of the pseudomorphic bcc Mg present in the layers. Among the multilayers where Mg is present in its hcp structure, the intermediate

thickness 8.4 nm/7.6 nm Nb/Mg multilayer has the largest volume fraction of bcc Mg, and hence this multilayer shows a mixture of hcp and bcc dominated responses under compression. For example, while the micro-compression deformation response of the 8.4 nm/7.6 nm Nb/Mg multilayer is more homogenous and does not exhibit the instability shown in the two larger Nb/Mg 14.1 nm/18.9 nm and 76.6 nm/62.6 nm layer thicknesses, the failure strain values of this multilayer is still smaller than those of the fully bcc Mg multilayers (Nb/Mg 1.7 nm/1.9 nm and 5.5 nm/5.5 nm, Table 2). As we increase the multilayer thickness, the volume fraction of bcc Mg become much smaller, and its effect becomes negligible. Thus, the deformation response of the two largest Nb/Mg layer thicknesses (Nb/Mg 14.1 nm/18.9 nm and 76.6 nm/62.6 nm) is dominated primarily by the hcp Mg phase present in these nanolaminates.

The TEM analysis of this Nb/Mg 8.4 nm/7.6 nm layer thickness (Fig. 2) also indicates that the critical layer thickness for the pseudo-morphic transformation is not a singular value but may manifest as a range of thicknesses over which the phase transformation gradually occurs. Interesting microstructurally complex microstructures are present, where the bcc pseudomorphic Mg phase forms a coherent interface with the Nb phase and an incoherent interface with the interior hcp Mg phase. These findings motivate further work into the underlying physics – such as the role of thin film stresses – behind the characteristic length scales governing the interface-driven pseudomorphic transformation in Mg.

Our study also helps to experimentally establish the correlation between indentation hardness and uniaxial yield in multilayered nanocomposites. Our results (Table 2) show that instead of a constant number, the hardness/yield stress ratio is strongly dependent on the plastic anisotropy of the multilayer components and the orientation of the loading axis during testing. For the three smaller Nb/Mg layer thicknesses (1.7 nm/1.9 nm, 5.5 nm/5.5 nm, and 8.4 nm/7.6 nm) the hardness/yield stress ratio varies between 2.32 to 2.62. In these cases, the deformation is dominated by the more plastically isotropic bcc Mg structure, and in our work the nanolaminate is tested in the isostress orientation (compression axis normal to the Nb/Mg interface planes). On the other hand, when the deformation response is dominated by the more plastically anisotropic hcp Mg component in the multilayer, a much lower ratio of 1.61 to 1.88 was measured for the two larger Nb/Mg 14.1 nm/18.9 nm and 76.6 nm/62.6 nm layer thicknesses. For these larger Nb/Mg layer thicknesses the compression loading axis was parallel to the c-axis of the hcp Mg layer present in the composite. Encouragingly, these ratios are relatively constant with changing layer thicknesses for the hcp Mg-dominated Nb/Mg multilayers

Both the uniaxial yield and hardness values are expected to vary for other loading orientations. For example, in the isostrain orientation (where the compression axis is parallel to the Nb/Mg interface planes) the uniaxial yield values have been reported to be lower $(1.14\pm0.04 \text{ and } 1.02\pm0.4 \text{ GPa}$ for the 5.5 nm/5.5 nm and 76.6 nm/62.6 nm layer thicknesses respectively [41]) than those shown in Table 2. Hardness values in the isostrain orientation were not measured in [41].

Over the past decades various attempts have been made towards predicting the hardness over uniaxial yield stress ratio [54-59] – see [60-62] for a detailed critique. Most of these studies have reported a (hardness/yield stress) factor of \sim 3 for elastic-perfectly plastic response, and multiple follow-up reports in literature have also use the factor of 3 for multilayered materials [1]. However, the results shown in Table 2 suggest caution before using a constant hardness/yield stress ratio for predictive purposes [62], especially in the case of anisotropic multilayered nanocomposites where different deformation mechanisms can be activated under uniaxial vs. multiaxial loading conditions.

5. Conclusions

In summary, our results reveal that the hcp-to-bcc pseudomorphic phase transformation of the Mg phase of Nb/Mg multilayered nanocomposites allows for concurrent improvements in both strength and strain-to-failure with decreasing layer thicknesses of the nanolaminates. Nb/Mg nanolaminates containing the bcc pseudomorphic Mg phase were found to have >60% higher strengths and >80% higher strain-to-failure values over those containing the traditional hcp Mg phase. This is a unique result and is in contrast with most literature reports on bi-metallic nanolaminates where the composite stress is known to plateau or even decrease below a certain layer thickness, and where such higher strengths are typically accompanied by a decrease in the mechanical stability of the composites. Our results suggest that the enhanced strength in Nb/Mg nanolaminates could be related to the change in interface character from an incoherent bcc/hcp interface to a coherent bcc/bcc one, which suppresses slip transmission and hence delays the underlying softening. Additional TEM investigations are needed to confirm this hypothesis.

Our HR-TEM results also provide important insights on the pseudomorphic hcp-to-bcc phase transformation process in Mg. Mg was found present in its pseudomorphic bcc structure for the two smaller Nb/Mg layer thicknesses of 1.7 nm/1.9 nm and 5.5 nm/5.5 nm, while the two largest Nb/Mg layer thicknesses (14.1 nm/18.9 nm and 76.6 nm/62.6 nm) had a thin layer of bcc Mg at the Nb/Mg interface, followed by hcp Mg. The thickness of the thin bcc Mg layer at the Nb/Mg interface was found to be slightly but consistently larger at the top of each individual Mg layer. The intermediate thickness Nb/Mg 8.4 nm/7.6 nm nanolaminate had a mix of both bcc and hcp Mg phases, and the bcc vs. hcp Mg phases were found to vary with changes in the total thin film thickness and the local film stresses present in the multilayer. These findings add to a growing body of work related to the underlying processes governing the interface-driven pseudomorphic transformation in Mg.

Our investigations reported similar values 0.2% offset yield stress values, stress at instability, strain at instability, as well as the general in-situ deformation behavior, between micro-pillars of square vs. circular cross-section shapes composed of Nb/Mg multilayers of various layer thicknesses and aspect ratios. These results suggest that either the square or the circular micro-pillar geometries can be used to reliably examine the micro-compression response in nanolaminates.

Additionally, the correlation between indentation hardness and uniaxial yield is established for the multilayered nanocomposites in this work. Interestingly, instead of a constant number, the hardness/yield stress ratios are found strongly dependent on the plastic anisotropy of the multilayer components and the orientation of the loading axis during testing.

Declaration of Competing Interest

The authors declare that they have no known competing financial interests or personal relationships that could have appeared to influence the work reported in this paper.

Acknowledgements

S.P. and M.J. acknowledge funding from NSF #2051443 and equipment funding from NSF MRI #1726897, ARO-DURIP #W911NF2110042 and DOE #DE-NE0008739 for this work. N.A.M. and I.J.B. acknowledge support by DOE BES DE-SC0020133 Office of Science, Basic Energy Sciences. This work was performed, in part, at the Center for Integrated Nanotechnologies, an Office of Science User Facility operated for the U.S. Department of Energy

(DOE) Office of Science by Los Alamos National Laboratory (Contract 89233218CNA000001) and Sandia National Laboratories (Contract DE-NA-0003525).

Supplementary materials

Supplementary material associated with this article can be found, in the online version, at doi:10.1016/j.actamat.2022.118487.

References

- A. Misra, J.P. Hirth, R.G. Hoagland, Length-scale-dependent deformation mechanisms in incoherent metallic multilayered composites, Acta Mater. 53 (18) (2005) 4817–4824.
- [2] I.J. Beyerlein, Z. Li, N.A. Mara, Mechanical Properties of Metal Nanolaminates, Annu. Rev. Mater. Res. 52 (1) (2022) 281–304.
- [3] H. Huang, F. Spaepen, Tensile testing of free-standing Cu, Ag and Al thin films and Ag/Cu multilayers, Acta Mater. 48 (12) (2000) 3261–3269.
- [4] T. Nizolek, I.J. Beyerlein, N.A. Mara, J.T. Avallone, T.M. Pollock, Tensile behavior and flow stress anisotropy of accumulative roll bonded Cu-Nb nanolaminates, Appl. Phys. Lett. 108 (5) (2016) 051903.
- [5] Q. Wei, D. Jia, K. Ramesh, E. Ma, Evolution and microstructure of shear bands in nanostructured Fe, Appl. Phys. Lett. 81 (7) (2002) 1240–1242.
- [6] D. Jia, K.T. Ramesh, E. Ma, Effects of nanocrystalline and ultrafine grain sizes on constitutive behavior and shear bands in iron, Acta Mater. 51 (12) (2003) 3495–3509.
- [7] E. Ma, Instabilities and ductility of nanocrystalline and ultrafine-grained metals, Scr. Mater. 49 (7) (2003) 663–668.
- [8] S. Cheng, E. Ma, Y.M. Wang, L.J. Kecskes, K.M. Youssef, C.C. Koch, U.P. Trociewitz, K. Han, Tensile properties of in situ consolidated nanocrystalline Cu, Acta Mater. 53 (5) (2005) 1521–1533.
- [9] M. Dao, L. Lu, R.J. Asaro, J.T.M. De Hosson, E. Ma, Toward a quantitative understanding of mechanical behavior of nanocrystalline metals, Acta Mater. 55 (12) (2007) 4041–4065.
- [10] C.C. Koch, Optimization of strength and ductility in nanocrystalline and ultrafine grained metals, Scr. Mater. 49 (7) (2003) 657–662.
- [11] N. Mara, I. Beyerlein, Review: effect of bimetal interface structure on the mechanical behavior of Cu-Nb fcc-bcc nanolayered composites, J. Mater. Sci. 49 (19) (2014) 6497-6516.
- [12] İ.J. Beyerlein, N.A. Mara, J.S. Carpenter, T. Nizolek, W.M. Mook, T.A. Wynn, R.J. McCabe, J.R. Mayeur, K. Kang, S. Zheng, J. Wang, T.M. Pollock, Interface-driven microstructure development and ultra high strength of bulk nanostructured Cu-Nb multilayers fabricated by severe plastic deformation, J. Mater. Res. 28 (13) (2013) 1799–1812.
- [13] I. Salehinia, S. Shao, J. Wang, H.M. Zbib, Plastic Deformation of Metal/Ceramic Nanolayered Composites, JOM 66 (10) (2014) 2078–2085.
- [14] S. Lotfian, C. Mayer, N. Chawla, J. Llorca, A. Misra, J.K. Baldwin, J.M. Molina-Aldareguía, Effect of layer thickness on the high temperature mechanical properties of Al/SiC nanolaminates, Thin Solid Films 571 (Part 2) (2014) 260–267.
- [15] S. Pathak, N. Li, X. Maeder, R.G. Hoagland, J.K. Baldwin, J. Michler, A. Misra, J. Wang, N.A. Mara, On the origins of hardness of Cu-TiN nanolayered composites, Scr. Mater. 109 (2015) 48–51.
- [16] T.P.D. Rajan, B.C. Pai, Developments in Processing of Functionally Gradient Metals and Metal-Ceramic Composites: a Review, Acta Metal. Sinica-Engl. Lett. 27 (5) (2014) 825–838.
- [17] X. Wu, Y. Zhu, Heterogeneous materials: a new class of materials with unprecedented mechanical properties, Mater. Res. Lett. 5 (8) (2017) 527–532.
- [18] J.H. Van Der Merwe, Crystal Interfaces. Part II. Finite Overgrowths, J. Appl. Phys. 34 (1) (1963) 123–127.
- [19] W.A. Jesser, A theory of pseudomorphism in thin films, Mater. Sci. Eng. 4 (5) (1969) 279–286.
- [20] S. Pathak, N. Velisavljevic, J.K. Baldwin, M. Jain, S. Zheng, N.A. Mara, I.J. Beyerlein, Strong, Ductile, and Thermally Stable bcc-Mg Nanolaminates, Sci. Rep. 7 (1) (2017) 8264.
- [21] B. Ham, X. Zhang, High strength Mg/Nb nanolayer composites, Mater. Sci. Eng. 528 (4–5) (2011) 2028–2033.
- [22] A. Junkaew, B. Ham, X. Zhang, A. Talapatra, R. Arróyave, Stabilization of bcc Mg in Thin Films at Ambient Pressure: experimental Evidence and ab initio Calculations, Mater. Res. Lett. 1 (3) (2013) 161–167.
- [23] A. Kumar, I.J. Beyerlein, J. Wang, First-principles study of the structure of Mg/Nb multilayers, Appl. Phys. Lett. 105 (7) (2014) 071602.
- [24] M. Jain, N. Velisavljevic, J.K. Baldwin, M. Knezevic, N.A. Mara, I.J. Beyerlein, S. Pathak, Structure and properties of pseudomorphically transformed bcc Mg in Mg/Nb multilayered nanolaminates studied using synchrotron X-ray diffraction, J. Appl. Phys. 126 (2) (2019) 025302.
- [25] A. Junkaew, B. Ham, X. Zhang, R. Arróyave, Tailoring the formation of metastable Mg through interfacial engineering: a phase stability analysis, Calphad 45 (Supplement C) (2014) 145–150.
- [26] J. Wang, M. Knezevic, M. Jain, S. Pathak, I.J. Beyerlein, Role of interface-affected dislocation motion on the strength of Mg/Nb nanolayered composites inferred by dual-mode confined layer slip crystal plasticity, J. Mech. Phys. Solids 152 (2021) 104421.
- [27] H. Olijnyk, W.B. Holzapfel, High-pressure structural phase transition in Mg, Phys. Rev. B 31 (7) (1985) 4682–4683.

- [28] G.W. Stinton, S.G. MacLeod, H. Cynn, D. Errandonea, W.J. Evans, J.E. Proctor, Y. Meng, M.I. McMahon, Equation of state and high-pressure/high-temperature phase diagram of magnesium, Phys. Rev. B 90 (13) (2014) 134105.
- [29] Y. Ogawa, D. Ando, Y. Sutou, J. Koike, A lightweight shape-memory magnesium alloy, Science 353 (6297) (2016) 368.
- [30] W. Xu, N. Birbilis, G. Sha, Y. Wang, J.E. Daniels, Y. Xiao, M. Ferry, A high-specific-strength and corrosion-resistant magnesium alloy, Nat. Mater. 14 (12) (2015) 1229–1235.
- [31] O. Pavlic, W. Ibarra-Hernandez, I. Valencia-Jaime, S. Singh, G. Avendaño-Franco, D. Raabe, A.H. Romero, Design of Mg alloys: the effects of Li concentration on the structure and elastic properties in the Mg-Li binary system by first principles calculations, J. Alloys Compd. 691 (2017) 15–25.
- [32] W. Wang, J. Foster, T. Snodgrass, A.E. Wendt, J.H. Booske, An rf sustained argon and copper plasma for ionized physical vapor deposition of copper, J. Appl. Phys. 85 (11) (1999) 7556-7561.
- [33] F. Medjani, R. Sanjinés, G. Allidi, A. Karimi, Effect of substrate temperature and bias voltage on the crystallite orientation in RF magnetron sputtered AlN thin films, Thin Solid Films 515 (1) (2006) 260–265.
- [34] X. Li, B. Bakhit, M.P.J. Jõesaar, L. Hultman, I. Petrov, G. Greczynski, Toward energy-efficient physical vapor deposition: routes for replacing substrate heating during magnetron sputter deposition by employing metal ion irradiation, Surf. Coat. Technol. 415 (2021) 127120.
- [35] Y. Gao, H. Bei, Strength statistics of single crystals and metallic glasses under small stressed volumes, Prog. Mater. Sci. 82 (2016) 118–150.
- [36] J.A. El-Awady, C. Woodward, D.M. Dimiduk, N.M. Ghoniem, Effects of focused ion beam induced damage on the plasticity of micropillars, Phys. Rev. B 80 (10) (2009) 104104.
- [37] D. Kiener, C. Motz, G. Dehm, Micro-compression testing: a critical discussion of experimental constraints, Mater. Sci. Eng. 505 (1–2) (2009) 79–87.
- [38] Z. Czigány, G. Radnóczi, Columnar growth structure and evolution of wavy interface morphology in amorphous and polycrystalline multilayered thin films, Thin Solid Films 347 (1) (1999) 133–145.
- [39] R.N. Tait, T. Smy, M.J. Brett, Modelling and characterization of columnar growth in evaporated films, Thin Solid Films 226 (2) (1993) 196–201.
- [40] C.R. Mayer, L.W. Yang, S.S. Singh, J. Llorca, J.M. Molina-Aldareguia, Y.L. Shen, N. Chawla, Anisotropy, size, and aspect ratio effects on micropillar compression of AlSiC nanolaminate composites, Acta Mater. 114 (2016) 25–32.
- [41] M. Ardeljan, M. Knezevic, M. Jain, S. Pathak, A. Kumar, N. Li, N.A. Mara, J.K. Baldwin, I.J. Beyerlein, Room temperature deformation mechanisms of Mg/Nb nanolayered composites, J. Mater. Res. 33 (10) (2018) 1311–1332.
- [42] T. Karabacak, J.J. Senkevich, G.-C. Wang, T.-M. Lu, Stress reduction in sputter deposited films using nanostructured compliant layers by high working-gas pressures, J. Vacuum Sci. Technol. A 23 (4) (2005) 986–990.
- [43] M.W. Kapp, A. Hohenwarter, S. Wurster, B. Yang, R. Pippan, Anisotropic deformation characteristics of an ultrafine- and nanolamellar pearlitic steel, Acta Mater. 106 (2016) 239–248.
- [44] K.M. Youssef, Y.B. Wang, X.Z. Liao, S.N. Mathaudhu, L.J. Kecskés, Y.T. Zhu, C.C. Koch, High hardness in a nanocrystalline Mg97Y2Zn1 alloy, Mater. Sci. Eng. 528 (25–26) (2011) 7494–7499.

- [45] E.N. Popova, V.V. Popov, E.P. Romanov, V.P. Pilyugin, Thermal stability of nanocrystalline Nb produced by severe plastic deformation, Phys. Metals Metallogr. 101 (1) (2006) 52–57.
- [46] H. Yu, Y. Xin, M. Wang, Q. Liu, Hall-Petch relationship in Mg alloys: a review, J. Mater. Sci. Technol. 34 (2) (2018) 248–256.
- [47] F.E. Hauser, P.R. Landon, J.E. Dorn, Fracture of magnesium alloys at low temperature, Trans. Am. Inst. Min. (Metall.) Eng. 48 (5) (1956) 589–593.
- [48] N. Ono, R. Nowak, S. Miura, Effect of deformation temperature on Hall-Petch relationship registered for polycrystalline magnesium, Mater. Lett. 58 (1) (2004) 39–43.
- [49] Z.C. Cordero, B.E. Knight, C.A. Schuh, Six decades of the Hall-Petch effect a survey of grain-size strengthening studies on pure metals, Int. Mater. Rev. 61 (8) (2016) 495–512.
- [50] C.H. Caceres, G.E. Mann, J.R. Griffiths, Grain Size Hardening in Mg and Mg-Zn Solid Solutions, Metal. Mater. Trans. A 42 (7) (2011) 1950–1959.
- [51] Y.Y. Lu, R. Kotoka, J.P. Ligda, B.B. Cao, S.N. Yarmolenko, B.E. Schuster, Q. Wei, The microstructure and mechanical behavior of Mg/Ti multilayers as a function of individual layer thickness, Acta Mater. 63 (2014) 216–231.
- [52] S. Subedi, I.J. Beyerlein, R. LeSar, A.D. Rollett, Strength of nanoscale metallic multilayers, Scr. Mater. 145 (2018) 132–136.
- [53] Y. Su, M. Ardeljan, M. Knezevic, M. Jain, S. Pathak, I.J. Beyerlein, Elastic constants of pure body-centered cubic Mg in nanolaminates, Comput. Mater. Sci. 174 (2020) 109501.
- [54] R. Hill, H.L. Eva, S.J. Tupper, F.M. Nevill, The theory of wedge indentation of ductile materials, Proc. R. Soc. Lond. Ser. A. Math. Phys. Sci. 188 (1013) (1947) 273–289.
- [55] Y. Tirupataiah, G. Sundararajan, On the constraint factor associated with the indentation of work-hardening materials with a spherical ball, Metal. Trans. A 22 (10) (1991) 2375–2384.
- [56] B. Taljat, T. Zacharia, F. Kosel, New analytical procedure to determine stress-strain curve from spherical indentation data, Int. J. Solids Struct. 35 (33) (1998) 4411–4426.
- [57] M. Beghini, L. Bertini, V. Fontanari, Evaluation of the stress-strain curve of metallic materials by spherical indentation, Int. J. Solids Struct. 43 (7) (2006) 2441–2459.
- [58] A. Ishlinsky, The three-dimensional plasticity problem and Brinell hardness test, J. Appl. Math. Mech.(USSR) 8 (3) (1944) 201–244.
- [59] K.L. Johnson, The correlation of indentation experiments, J. Mech. Phys. Solids 18 (2) (1970) 115–126.
- [60] D.K. Patel, S.R. Kalidindi, Correlation of spherical nanoindentation stress-strain curves to simple compression stress-strain curves for elastic-plastic isotropic materials using finite element models, Acta Mater. 112 (2016) 295–302.
- [61] B.R. Donohue, A. Ambrus, S.R. Kalidindi, Critical evaluation of the indentation data analyses methods for the extraction of isotropic uniaxial mechanical properties using finite element models, Acta Mater. 60 (9) (2012) 3943–3952.
- [62] M.D. Gram, J.S. Carpenter, P.M. Anderson, An indentation-based method to determine constituent strengths within nanolayered composites, Acta Mater. 92 (2015) 255–264.